Revision 2

Influence of grain size, water and deformation on dolomite reaction rim formation

VANESSA HELPA[1], ERIK RYBACKI[1], LUIZ FERNANDO GRAFUHLA MORALES[1], GEORG DRESEN[1]

[1]Deutsches GeoForschungsZentrum GFZ, Telegrafenberg, 14473 Potsdam, Germany

Vanessa Helpa: Helpa@gfz-potsdam.de

Erik Rybacki: Uddi@gfz-potsdam.de

Luiz Morales: Morales@gfz-potsdam.de

Georg Dresen: Dre@gfz-potsdam.de

ABSTRACT

Solid-solid mineral reaction rates are influenced by the microfabrics of reactant phases and concurrent deformation. To investigate this interplay in carbonate systems, we performed annealing and deformation experiments on polycrystalline and single crystal calcite and magnesite, forming dolomite (Dol) and magnesio-calcite (Mg-Cal). At a fixed temperature of $T = 750$ °C and confining pressure of $P = 400$ MPa, samples were either annealed for 29 h, or deformed in triaxial compression or torsion for 18 h using a Paterson-type gas deformation apparatus. At the contact interface of the starting reactants, Dol reaction rims and polycrystalline Mg-Cal layers were formed. The widths of the layers were in the ranges 4-117 µm and 30-147 µm, respectively, depending on the microstructure of starting materials and experimental conditions. Annealing experiments with polycrystalline reactants in contact with each other resulted in a ~22-fold increase in Dol rim thickness compared to a contact between two single crystals and a larger Mg-Cal layer width by a factor of 5 (cf. Helpa et al. 2014). This suggests that the microstructure of magnesite controls migration of the reaction front. For polycrystalline starting materials, axial stress accelerated Mg-Cal growth rates but not Dol growth rates. Highly strained torsion samples showed Dol formation along grain boundaries in Mg-Cal as well as in the polycrystalline calcite reactant. A reduction of Dol rim thickness between polycrystalline reactants deformed in torsion is possibly caused by concurrent grain coarsening of polycrystalline magnesite. Dol and Mg-Cal growth kinetics between single crystals were unaffected by the addition of ~0.3 wt% water.

The experiments demonstrate that Dol reaction kinetics strongly correlate with magnesite reactant grain sizes, while Mg-Cal growth depends on the calcite reactant grain sizes. The dolomite-forming mineral reaction kinetics are not significantly affected by concurrent deformation. In contrast, deformation enhances Mg-Cal formation, especially at small calcite grain sizes that promote efficient grain boundary diffusion.

Therefore, the fastest reactions forming Dol and Mg-Cal in nature are expected to occur in very fine-grained reactants. Concurrent deformation may drastically enhance reaction kinetics if grain size reduction of the reactants occurs by, for example, cataclasis or dynamic recrystallization.

Keywords Rim growth · carbonates · diffusion · deformation · water

INTRODUCTION

In nature, metamorphic rocks often exhibit evidence of simultaneous deformation and mineral reactions (e.g., Rubie 1983; Rutter and Brodie 1988; Newman et al. 1999 and references therein). Evidence for the concurrent occurrence of these processes is well documented in natural mylonites (Rubie 1983; Fitz Gerald and Stünitz 1993; Newman et al. 1999; Tsurumi et al. 2003). The results of laboratory experiments addressing syn-deformational reactions suggest a correlation between mineral reactions and deformation in several mineral systems (e.g., de Ronde et al. 2004, 2005; Holyoke and Tullis 2006; de Ronde and Stünitz 2007). In silicate systems, the presence of small amounts of water drastically accelerates deformation and reaction rates (e.g., Post et al. 1996; Hirth et al. 2001; Rutter and Brodie 2004; Gardés et al. 2012; Milke et al. 2013). In contrast, the effect of water on deformation in carbonate systems is minor (de Bresser et al. 2005).

Here, we study the calcite ($CaCO_3$) – magnesite ($MgCO_3$) carbonate system, which produces dolomite ($CaMg(CO_3)_2$) following the overall reaction:

$$CaCO_3 + MgCO_3 = CaMg(CO_3)_2 \tag{1}$$

The partial reactions at the reactant interfaces are described by Helpa et al. (2014) (their equations 2 and 3). Formation of dolomite is associated with a negative volume change of ≈-12% at the calcite interface and a positive volume change of ≈+14% at the contact with magnesite. Between stoichiometric dolomite and pure calcite, a continuous exchange of Ca and Mg produces magnesio-calcite ($Ca_{1-x}Mg_xCO_3$) and a non-stoichiometric dolomite. Previous experimental studies of this reaction using calcite and magnesite single crystals under isostatic and non-isostatic conditions revealed a diffusion-controlled dolomite reaction rim growth, which was almost unaffected by applied axial stresses up to 38 MPa, but slightly reduced at high strain rates (Helpa et al. 2014, 2015).

In this study, annealing and deformation experiments were performed on single crystals and polycrystalline starting materials with the goals of (1) determining the effect of polycrystalline starting materials in the formation of dolomite in calcite-magnesite diffusion couples under isostatic conditions as well as under axial and torsion deformation, and (2) determining whether dolomite formation significantly depends on the presence of excess water.

MATERIALS AND EXPERIMENTAL METHODS

Starting materials

We used natural single crystals and polycrystalline calcite and magnesite for the starting assembly. Calcite (Brazil, Minas Gerais) and magnesite (Brazil, Bahia Brumado) single crystals were optically clear with a rhombohedral habit. Chemical compositions of single crystals were obtained by 8-10 point measurements using a field-emission electron microprobe (JEOL JXA-8500 F HYPERPROBE) at 15 keV accelerating voltage, 5 nA beam current, and 15 µm beam diameter with a counting time of 20 s on peak. These results indicated relatively pure single crystals with minor impurities of 0.17 wt% Ba in calcite as well as 0.15 wt% Fe and 0.23 wt% Ca in magnesite.

Solnhofen limestone (Germany), Lorrano Bianco marble (Italy, Carrara) and magnesite from Zimbabwe (Africa) were used as polycrystalline starting material. Average grain sizes and porosities were determined by the line-intercept method (Underwood 1970). Mineralogical compositions of the polycrystalline starting materials were determined by powder X-ray diffraction (XRD) using a STOE Stadi P diffractometer with CuKα radiation (λ = 1.5405 Å). Data were collected from 5 to 125 ° 2θ, at a counting rate of 0.01 ° 2θ s^{-1}. Water contents of the starting materials were measured using a Vario EL III element analyzer (Elementar Analysesysteme GmbH).

Solnhofen limestone has an average grain size of 6(1) µm (1 standard deviation in parentheses here and elsewhere) and 4% porosity. It is nearly pure $CaCO_3$ containing only minor amounts of Mg in solid solution. The corresponding mole fractions for calcium and magnesium are Ca/(Ca+Mg) = X_{Ca} = 0.994 and molar Mg/(Ca+Mg) = X_{Mg} = 0.006, respectively. The measured water content ranges between 0.4 and 0.58 wt%. Carrara marble is composed of calcite with $X_{Ca} \geq 0.99$, a porosity of < 0.5%, a random crystallographic preferred orientation (CPO), and an average grain size of 220(40) µm (Rybacki et al. 2013). The estimated water content is ≈ 0.4-0.6 wt%. Polycrystalline magnesite is fine-grained (≈ 4 µm) with a porosity of about 6%. Some small dolomite grains are randomly distributed in the matrix or form small veins. The amount of dolomite in the magnesite matrix is less than 4%. XRD measurements revealed a bulk composition of X_{Mg}= 0.95 and X_{Ca} = 0.05. The determined water content ranges between 0.4-0.58 wt%.

Sample assemblies were cylinders with 7 mm diameter and 2.5-4.8 mm length composed of various stacks of starting materials. Single crystal cylinders were cored perpendicular to the natural cleavage planes and Solnhofen limestone cylinders were cored perpendicular to the bedding. The end faces of the cylinders were subsequently polished to ensure a good contact between the reactants. Solnhofen limestone contains a weak initial CPO with **c**-axes oriented parallel to the bedding plane (Llana-Fúnez and Rutter 2014). To evaluate the effect of starting material microstructure on reaction progress in a single run, we stacked single crystal and polycrystalline cylinders in different combinations (**Table 1**). In the following we will use abbreviations as defined in **Table 1**.

Experimental procedure

All experiments were performed using a Paterson-type gas deformation apparatus at a fixed temperature of T = 750 °C, a confining pressure of P = 400 MPa and run durations of t = 18 h for triaxial compression and torsion experiments, and 29 h for static annealing experiments (**Table 1**). Shorter run durations for deformation experiments were chosen because of the relatively fast deformation of polycrystalline starting materials. Experiments were performed following the procedure described by Helpa et al. (2015).

Three annealing experiments were performed on different reactant stacks using samples with natural (as-is) water content. In addition, one annealing experiment was done with a modified assembly (Ca_Mg_Dia-01) to examine the role of water on mineral reaction between two single crystals. For this experiment, a 2.3-mm-diameter borehole was drilled in the center of the Mgs parallel to the cylindrical axis and filled with diaspore (AlOOH). At a confining pressure of 400 MPa, diaspore dehydrates to corundum (Al_2O_3) at $T \approx 420$ °C (Haas 1972), releasing around 15 wt% H_2O.

One triaxial compression experiment was conducted at a constant stress of $\sigma = 20$ MPa to investigate the effect of coaxial stress on the rim growth behavior. After yielding, the sample stack deformed at a bulk rate of about 1×10^{-4} s^{-1} to a bulk strain of 0.17 within about 0.5 h. Subsequently, the assembly was annealed for 17.5 h to allow comparison with torsion experiments. To evaluate the influence of high strain deformation on the reaction, two torsion experiments were performed at a constant twist rate of ~7×10^{-5} s^{-1} to maximum shear strains at the cylinder periphery of $\gamma = 2$ and 4 (**Table 1**). Since deformation was mainly partitioned into the (weak) polycrystalline reactant phases, strain here refers to the length of the corresponding starting samples. For determination of the maximum shear stress from the measured torque, we assumed power law creep behavior with a stress exponent of 1.66 and 1.1 for Soln limestone and poly-Mgs, respectively (Schmid et al. 1977; Holyoke et al. 2014). For experiment pCa_pMg-01 with polycrystalline starting materials, the shear stress was 1.7 ± 0.4 MPa up to a shear strain of 0.6, followed by strain hardening to a maximum shear stress of 3.8 ± 0.5 MPa at $\gamma = 2$. For experiment Ca_pMg-02 with Cal and poly-Mgs as starting materials the shear stress of 1.7 ± 0.4 MPa was constant up to $\gamma = 4$. In this high strain experiment, wrinkles on the copper jacket indicate partial deformation of the Cal (≈0.5 mm wide), associated with twins and cleavage cracks orientated parallel to natural cleavages.

Mechanical data were corrected for the strength of the copper jackets and system compliance. The reported errors in stress result from uncertainty in the jacket strength. After experiments, sample assemblies were cut along the cylindrical axis, embedded in epoxy and polished for analysis of the reaction products. In addition, tangential thin sections were prepared from twisted samples, cut parallel to the cylindrical axis close to the outer periphery.

Analytical methods

The layer thicknesses of the reaction products and their grain sizes were analyzed using an optical microscope (Leica DM RX) with an attached high-resolution digital camera (Leica DFC 420). For determination of rim/layer thickness, a set of reflected-light micrographs along the entire reaction interface was collected and phase boundaries were redrawn by hand. In experiments with polycrystalline starting material, phase boundaries were identified petrographically by a change in microstructure and/or grain size. The average reaction layer thicknesses were calculated from digitized traces of the phase boundaries. Grain sizes of reaction products were estimated by measuring the size of 50 individual grains within each layer and subsequently averaged (Joachim et al. 2010).

Using an electron microprobe, the distributions of major elements Ca ($K\alpha$, PETJ) and Mg ($K\alpha$, TAP) across the reaction products were investigated. Line scans of wavelength dispersive X-ray analyses were collected at an accelerating voltage of 15 keV, a beam current of 2 nA and a counting time of 20 s on each peak. To avoid beam damage to the carbonates, a beam diameter of 2 μm and a step size of 2 μm were used for point measurements. XRD measurements were converted to concentrations of Ca and Mg using the Rietveld refinement method. Crystallographic orientation relations between reactants and reaction products were investigated by a combination of electron backscatter diffraction (EBSD, TSL DigiView) and semi-quantitative energy dispersive spectroscopy (EDS). Operating details and evaluation procedures are described by Helpa et al. (2014).

RESULTS

In all experiments a coarse-grained magnesio-calcite (Mg-Cal) layer and a fine-grained dolomite (Dol) reaction rim developed at the initial contact interface of the starting reactants. The microstructures and thickness of reaction products strongly depend on starting material microstructure.

Thickness of reaction product layers

Annealing experiments. The optically measured Dol rim and Mg-Cal layer thicknesses and grain sizes from all experimental samples are summarized in **Table 2**. Considering the initial content of $X_{Ca} = 0.05$ in polycrystalline magnesite and $X_{Mg} = 0.006$ in Solnhofen limestone, the optically measured thicknesses of magnesite-grown Dol ($\Delta x_{Dol\text{-}Mgs}$) and calcite-grown Dol ($\Delta x_{Dol\text{-}Cal}$) represent upper limits. Correction for the pre-existing concentrations of Mg and Ca would lower the measured thicknesses by around 5% and 0.6% for $\Delta x_{Dol\text{-}Mgs}$ and $\Delta x_{Dol\text{-}Cal}$, respectively. After annealing, the reaction layer thicknesses are considerably higher for polycrystalline than for single crystal starting materials (**Fig. 1**). For example, in sample stack-01 the entire Dol layer thickness ($\Delta x_{Dol} = \Delta x_{Dol\text{-}Cal} + \Delta x_{Dol\text{-}Mgs}$) for two polycrystalline reactants ($\Delta x_{Dol} \approx 108$ µm) is nearly twice that of two single crystal reactants ($\Delta x_{Dol} \approx 47$ µm) (**Fig. 1**). The Mg-Cal layer thickness is $\Delta x_{Mg\text{-}Cal} \approx 130$ µm and $\Delta x_{Mg\text{-}Cal} \approx 41$ µm for polycrystalline and single crystal reactant phases, respectively. Using combinations of polycrystalline and single crystal starting materials yields remarkably different results. Poly-Mgs in contact with Cal results in a Dol rim thickness of $\Delta x_{Dol} \approx 98$ µm, but a Mg-Cal layer thickness of only $\Delta x_{Mg\text{-}Cal} \approx 52$ µm i.e. half as much as measured between two polycrystalline starting materials. The smallest Dol rim of $\Delta x_{Dol} \approx 5$ µm was measured between Soln in contact with a Mgs (**Fig. 1**).

Experiment pCa_Mg_pCac-01 gives a similar result for Dol ($\Delta x_{Dol} \approx 5$ µm) produced between Soln and Mgs, but a thicker Dol rim of $\Delta x_{Dol} \approx 9$ µm when coarse-grained Carrara is used instead of fine-grained Soln (**Fig. 1**). Carrara in contact with poly-Mgs (experiment pCa_pMg_pCac-01) yields approximately the same Dol rim width as obtained between Soln and poly-Mgs (108-117 µm), but a different width of Mg-Cal. In between Carrara and poly-Mgs the Mg-Cal layer is ~65 µm thick, while it ranges between 106–147 µm when Soln and poly-Mgs are used (cf. **Table 2, Fig. 1**). The thicknesses of Dol and Mg-Cal for Mgs in contact with Carrara are ≈9 µm and ≈30 µm, respectively. This is roughly comparable to the results obtained between single crystals ($\Delta x_{Dol} \approx 13$ µm and $\Delta x_{Mg\text{-}Cal} \approx 32$ µm, Helpa et al. 2014, **Fig. 1**). Excess water provided by dehydration of diaspore (experiment Ca_Mg_Dia-01) yields comparable results for two single crystals in contact ($\Delta x_{Dol} \approx 14$ µm and $\Delta x_{Mg\text{-}Cal} \approx 37$ µm). However, between the Mgs and Cal of sample stack-01, the layers are distinctly thicker with $\Delta x_{Dol} \approx 47$ µm and $\Delta x_{Mg\text{-}Cal} \approx 41$ µm.

Deformation experiments. The effect of deformation on reaction progress is shown in **Figure 2**. As in the annealing experiments, the reaction layers are much thicker for poly-Mgs compared to Mgs, but layer growth is hardly affected if Cal single crystals are used instead of poly-Cal (**Table 2**). However, the reaction layer width obtained in triaxial compression leads to thinner Dol rims when poly-Mgs is used. For direct comparison of the deformation experiments with those of annealed samples, Dol rim and Mg-Cal layer widths were corrected from those after actual run durations of t = 29 h to width expected for t = 18 h. Expected values for the Dol rims were derived assuming a parabolic rim growth behavior. Since the Mg-Cal layer initially does not grow linearly with the square root of time, growth rates reported by Helpa et al. (2014) for a Mg-Cal layer between single crystals were used to determine the expected layer widths. Thus, the entire Dol rim thickness between poly-Mgs and a Cal is estimated at only ~65 µm in deformed samples compared to ~77 µm in annealed samples after 18 h. Mg-Cal layers have similar widths around ~43 μm. In between poly-Mgs and fine-grained Soln the effect is more pronounced with thicknesses of ~67 μm and ~85 μm for the triaxially compressed sample compared to the annealing experiment. However, the Mg-Cal layer is significantly larger in deformed samples with $\Delta x_{Mg\text{-}Cal} \approx$ 69 μm, compared to the expected width of $\Delta x_{Mg\text{-}Cal} \approx$ 46 μm for static annealing. With two single crystal starting reactants, no influence of deformation was observed on the reaction product growth (Helpa et al. 2015). The same Dol rim thickness of $\Delta x_{Dol} \approx$ 4 μm, and similar Mg-Cal layer thicknesses of 27 and 32 μm were observed between Mgs and Soln (**Fig. 2**). Comparison of samples deformed to low axial strain and to high shear strains in torsion shows that the width of Dol rims between Soln and poly-Mgs is reduced by 30% in torsion, whereas the Mg-Cal layer is not affected. Similarly, in torsion a reduction of Δx_{Dol} between Cal and poly-Mgs is observed, but an increase of 23% for the Mg-Cal layer thickness occurs.

Microstructures of reaction products

Static annealing microstructures. Dol rims produced between polycrystalline starting materials are composed of elongated grains on both sides of the initial contact interface, oriented perpendicular to the interface (**Fig. 3a, b**). The initial interface is estimated from the presence of a granular Dol layer just a few grains thick, located at the center of the Dol rim (**Fig. 3b**). This microstructural boundary within Dol is comparable to the boundary between elongated and granular Dol at the initial interface observed in annealing experiments of single crystal starting materials (Helpa et al. 2014). Elongated Dol grains in contact with poly-Mgs show slightly curved grain boundaries and contain isolated inclusions of magnesite. Boundaries of Dol grains next to Mg-Cal are irregular in shape with little or no evidence of inclusions. Large Mg-Cal grains show curved boundaries with low porosity, often associated with Dol formation.

The microstructure of Dol is quite similar for Dol between poly-Mgs and Cal reactants (**Fig. 3c, d**). The Mg-Cal layer contains no porosity and is composed of small numbers of large grains with curved boundaries (**Fig. 3c, d)**. Dol grown between two single crystals exhibits two distinct microstructural domains (**Fig. 3e, f**). Elongated, palisade-shaped Dol grains grown into magnesite are characterized by relatively straight grain boundaries, often containing inclusions of magnesite. In the center of the rim, Dol grains are equidimensional with slightly curved but regular grain boundaries, which are more irregular in contact with Mg-Cal. Large Mg-Cal grains increase in size from the Dol boundary towards pure Cal with mostly straight or gently curved grain boundaries, often forming 120° triple junctions. The microstructures of Dol and Mg-Cal that evolved between single reactant crystals at water saturated conditions due to dehydration of diaspore (experiment Ca_Mg_Dia-01) are similar, albeit with more irregular grain boundaries in both Dol domains.

Microstructures of thin Dol rims between Mgs and fine-grained Soln are weakly developed; locally the reaction rim is a layer of single dolomite grains (**Fig. 3g**). Mg-Cal grains next to the Dol reaction rim are slightly coarser compared to the grain size of the Soln reactant. Dol also formed at grain boundaries and pores within the Mg-Cal layer (**Fig. 5b**). Using coarse-grained Carrara marble as starting material produced straighter or only slightly curved Dol grain boundaries, as for those observed between two single crystals.

The average grain size of Dol (≈5-6 μm) and of Mg-Cal (≈20-25 μm) are independent of the starting material except between Mgs and Carrara, where Dol grain size is distinctly smaller (**Table 2**).

Deformation microstructures. The microstructures of the reaction products deformed in triaxial compression are similar to those developed in static annealing experiments.

However, in torsion experiments, strain partioning into the Dol reaction rim is apparent from the microstructure. Dol grains next to magnesite between two polycrystalline reactants are slightly elongated**,** whereas calcite-grown Dol grains are more equiaxed or partially flattened parallel to the shear plane. Grain boundaries are more often curved or irregular compared to the grains in contact with magnesite. Similarly to the annealing experiments, Dol formed around pores within the Mg-Cal layer (**Fig. 4**). Interestingly, Dol also decorates grain boundaries in Soln up to a distance of at least 100 µm from the reaction interface between the limestone and Mg-Cal (**Fig. 4**). Inspection of tangential thin sections reveals a tilting of the long axis direction of elongated Dol grains towards the direction of shear.

Dol grains next to magnesite produced between Cal and poly-Mgs are slightly elongated with straight boundaries in the high strain region, while equiaxed Dol grains have straight or slightly curved boundaries in the center of the Dol rim. Close to Mg-Cal and Dol phase boundaries, grains are tilted towards the direction of shear and grain boundaries are highly irregular.

Twisted samples contain a thin Mg-Cal layer between the copper jacket and the calcite reactant phase, in particular along the Cal reactant, revealing a high mobility of Mg in the highly strained portion of samples.

Texture analysis

In static annealing experiments with two single crystals in contact, all reaction products show at least an axiotactic (one crystallographic axis parallel) relation with respect to Cal, similar to the results of a previous study (Helpa et al. 2014). In contrast, Dol formed in contact with polycrystalline starting material shows no crystallographic relationship to the reactant phases. Nevertheless, a crystallographic preferred orientation (CPO) developed, characterized by [0001] axes forming girdles lying within the reaction interface and poles of $\{2\bar{1}\bar{1}0\}$ and

$\{10\bar{1}0\}$ prismatic planes arranged (sub-) parallel to the growth direction (GD). $\{10\bar{1}4\}$ poles are blurred and widely distributed over the pole figures.

In deformed samples, CPO's of the reaction products evolved independently of the starting materials and their crystallographic orientations. The CPOs of the reaction products are controlled by the orientation of the maximum principle stress. This was also reported by Helpa et al. (2014). For example, torsion experiments feature [0001] axes forming oblique girdles at around 45° to the reaction interface, with a maximum between the GD and the center of the net. The poles of the prismatic planes are inclined to the reaction interface (shear plane), but in a direction opposite of the [0001] axes. The Mg-Cal layer contains a CPO with the [0001] maximum parallel to the shear direction. Other secondary maxima are spread over the pole figures, with poles of prism and rhombohedral planes forming clusters.

Microprobe analysis

Chemical profiles across the reaction products after static annealing and high strain torsion are shown in **Figures 5** and **6**. Single crystal reactants have homogenous compositions indicated for $X_{Ca} \approx 1$ in Cal and $X_{Mg} \approx 1$ in Mgs. Spikes in the chemical profiles of polycrystalline starting materials correspond to impurities and pores (**Fig. 5b**). Generally, a nearly stoichiometric composition is achieved in Dol from the initial contact interface to the magnesite reactant (**Figs. 5, 6**). At the interface with magnesite, Dol contains 52 mol% of an Mg component, which is slightly higher than the expected value of $X_{Mg} = 0.51$ for local equilibrium with magnesite. Local deviations in the Dol concentration profiles are attributed to isolated magnesite inclusions within poly-Mgs reactants (**Figs. 5, 6**). Calcite-grown Dol has an excess of the Ca component, continuously increasing towards the Mg-Cal boundary. At the interface to Mg-Cal, Dol has $X_{Mg} = 0.43\text{-}0.45$ which is significantly lower than the local equilibrium of $X_{Mg} = 0.48$. This may be associated with the accuracy of measurements performed on 2D sections that can be biased by undetected variations of the microstructure in the 3rd dimension. However, a depletion of the Mg component with respect to the local equilibrium was established in all measured concentration profiles. For the Mg-Cal layer, a successive decrease is observed in the Mg component from the Dol boundary towards pure calcite. Starting from a calcite single crystal, the decreasing Mg content correlates with an increase in grain size. Small peaks in the chemical profiles are caused by pores at grain boundaries, accompanied by some Dol formation, if Soln or Carrara marble is used as starting material.

In the central low strain ($\gamma \approx 0.1$) part of the twisted sample stack Ca_pMg-02, the element distributions of Ca and Mg are comparable to those of the annealed sample (**Fig. 6a**). In contrast, at intermediate ($\gamma \approx 1.9$) and high ($\gamma \approx 3.4$) strain conditions, constant mole fraction values are observed on both sides adjacent to the Dol/Mg-Cal boundary (**Fig. 6b, c**), probably induced by high phase boundary mobility.

DISCUSSION

Influence of chemistry and microstructure on reaction progress

Diffusion-controlled solid reaction rim growth is limited by the transport of matter from one reaction front to the other. Two different pathways are available: volume diffusion through the crystal lattice or diffusion along grain boundaries. Grain boundary diffusion is usually several orders of magnitudes faster compared to volume diffusion and operates on larger spatial scales (Dohmen and Milke 2010). Depending on grain size, a combination of these two transport processes yield an effective diffusion rate. It is commonly assumed that diffusion of the slowest species along its fastest path is rate-limiting and controls the overall effective growth rate. For Dol rim growth between Cal and Mgs under isostatic conditions, counter-diffusion of Ca and Mg was inferred to be rate-controlling (Helpa et al. 2014). Unfortunately, the determined diffusion coefficients ($D_{CaO,MgO} \approx 10^{-14}$ m/s²) in dolomite did not allow discrimination between predominant volume or grain boundary diffusion at these conditions.

In this study, mass balance considerations are based on the position of the initial contact interface, the measured reaction layer thicknesses and the measured chemical profiles (**Table 2; Fig. 5, 6**). Analyzes showed that the molar amount of Mg (n_{Mg}) transferred across the initial interface is always higher than the amount of Ca (n_{Ca}), as given by the fraction ν_{Mg}:

$$v_{Mg} = \frac{n_{Mg}}{n_{Mg}+n_{Ca}} \qquad (2)$$

Calculated values are given in **Table 2**. Nevertheless, it is likely that most of the mass transport occurs by Ca^{2+} and Mg^{2+} counter-diffusion, because it is the energetic most favorable way for dolomite formation based on the similar crystal structures of carbonates. The significant greater Mg^{2+} transport in some experiments and the formation of Mg-Cal at the contact between samples and the copper jacket in the torsion experiments, indicate a second transport mechanism. This likely involved solution, reprecipitation, and mass transport of Ca^{2+}, Mg^{2+}, and CO_3^{2-} (or possibly other equivalent species) in some kind of fluid. The assumption of a second transport mechanism is supported by an increasing ratio of $\Delta x_{Dol-Mgs}/\Delta x_{Dol-Cal}$ with increasing temperature up to $\Delta x_{Dol-Mgs}/\Delta x_{Dol-Cal} \approx 0.6$ at 850°C (Helpa et al. 2014).

Chemical profiles reveal a sharp step in the Ca/Mg distribution at the Dol-Mgs reaction front, in good agreement with local equilibrium conditions for Mgs in contact with Dol (**Fig. 5, 6**). No chemical gradients are observed in Mgs and Dol close to the interface, similar to those present at the Dol-Mg-Cal interface. At the experimental conditions, magnesite ought to incorporate $X_{Ca} \approx 0.017$ of the Ca component. Thus, it is likely that chemical gradients are present, but are too small or too local to be determined. At the Dol-Mg-Cal interface, the composition of calcite-grown Dol is not stoichiometric, with progressive decrease in X_{Mg} towards the Mg-Cal phase (**Fig. 5, 6**), which likely affects chemical exchange and interface migration. Furthermore, the formation of the Mg-Cal layer requires a longer diffusion pathway of the Mg component into the calcite reactant compared to transport of the Ca component into Mgs. This suggests a relatively fast Mg diffusion coefficient. The difference in mobility between Mg and Ca is likely caused by the relatively large ionic radius of Ca (0.99 Å) compared to the relatively small Mg ionic radius of 0.66 Å (Althoff 1977). With respect to the unit cell volumes of $V_{Cal} = 367.91$ Å^3 and $V_{Mgs} = 279.13$ Å^3 (Deer et al. 1992), mobility of small Mg point defects in the Cal lattice should be higher than mobility of large Ca point defects in Mgs. Our results demonstrate that the grain size of the magnesite starting material has an important influence on the Dol reaction rim formation. Annealing experiments revealed that the Dol layer is considerably thicker if fine-grained poly-Mgs is used as starting material (**Fig. 1**). In addition, dolomite-dolomite grain boundaries in experiments with poly-Mgs are oriented parallel to the diffusive fluxes, possibly promoting fast mass transport along grain boundaries and enhanced reaction progress (**Fig. 3 a-d**). Moreover, Dol grown into poly-Mgs contains isolated inclusions of magnesite within individual Dol grains. The magnesite inclusions are smaller next to the initial interface than at the Dol-magnesite reaction interface (**Fig. 4, 5, 6**). We interpret the inclusions as residual magnesite that is progressively consumed by Dol as the reaction proceeds in time. The inclusions and the thicker Dol rim evolving in poly-Mgs compared to Mgs suggests that reorganization of the crystal lattice may control the complete Dol transformation. The width of the entire Dol rim is hardly affected by the grain size of the calcite stating material (≈7 mm for Cal, 220 μm for Carrara and 6 μm for Soln). In contrast the reaction front mobility is controlled by the diffusion of Ca along grain boundaries in magnesite.

The thickness of the Mg-Cal layer increases continuously with decreasing grain size of the calcite reactant (**Fig. 1**). This suggests that formation of Mg-Cal is controlled by grain boundary diffusion of the Mg component into calcite to form Mg-Cal.

Counter-diffusion of Ca towards the Dol interface along grain boundaries of Cal is significantly faster than diffusion of Ca within Cal grain interiors. This is in agreement with results from Farver and Yund (1996) for Ca diffusion along grain boundaries and through the crystal lattice. We expect diffusion to be rapid along interconnected pores as well, as suggested by the presence of Dol along pores within the Mg-Cal layer in contact with Soln. The pores are preferentially located at triple junctions and grain boundaries (**Fig. 4, 5b**). Pores are more likely interconnected in the limestone with 4% porosity compared to marble with <0.5% porosity.

Influence of deformation on reaction progress

Reaction progress involving dolomite formation and Mg-Cal layer growth is significantly affected by deformation. Dol reaction rims between poly-Mgs in contact with Cal are 15% thinner in triaxially compressed samples and 39% thinner in twisted samples compared to the annealing experiment. The width of the Mg-Cal layer formed in Cal is not affected by triaxial compression, but is about 23% larger in torsion experiments.

The effect of deformation is even more pronounced if poly-Mgs and Soln are used as reactants. Triaxial compression leads to 21% thinner dolomite rims and torsion lowers the Dol rim width by about 45%. In contrast, triaxial compression and torsion of starting materials produce Mg-Cal layers, which are about 50% thicker than during static annealing.

In summary, the reaction rates of Dol formation are reduced if samples are simultaneously annealed and deformed, irrespective of total strain. Rates of Mg-Cal formation are either unaffected or increased.

Helpa et al. (2015) found that stresses up to 38 MPa do not alter the reaction rate of Dol and do not significantly change the thermodynamic driving forces. These authors also observed an enhanced rate of Mg-Cal production at high strains (>0.1), which was attributed to enhanced dislocation activity that provided additional diffusion pathways. Our results are consistent with these conclusions. Deformation may also increase the mobility of grain boundaries and grain boundary diffusion rates, leading to Dol formed along grain boundaries in Mg-Cal and Soln in highly strained torsion samples.

For poly-Mgs starting material, the Dol rim thickness in deformed samples is thinner compared to annealed samples. The average grain sizes of the involved polycrystalline phases are given in **Table 3**, demonstrating grain growth to similar final grain sizes after 29 h of annealing or 18 h of deformation. The faster grain growth in deformation experiments may influence the reaction progress by reducing the grain boundary density. This would be an important parameter if grain boundary diffusion is predominant. Assuming a grain growth law of the form

$$d^n - d_0^n = Kt \tag{3}$$

with d_0 = initial grain size, d = final grain size after time t, K = rate constant and n = 2-3 (Olgaard and Evans 1986, 1988; Covey-Crump 1997), the grain size of magnesite can be back-calculated from 29 to 18 h annealing time, resulting in a size of ≈9.0-9.5 μm. If we further neglect the Mg-Cal formation and assume for simplicity that the effective diffusivity D is inversely proportional to the grain size d and proportional to the square of rim thickness (i.e., $(\Delta x_{Dol})^2 \sim D \sim d^{-1}$, Gardés et al. 2011), then the predicted reduction in Dol rim thickness between annealed and triaxially deformed samples is about 7-10%, depending on the assumed grain growth exponent n. Within error, this agrees with the observed reduction of ≈14%.

Influence of water on reaction

In experiment Ca_Mg_Dia-01, dehydration of diaspore increases the water content of the starting materials by about 0.3 wt%, if all released water is incorporated into the single crystal reactants. Measured average thicknesses of Dol and Mg-Cal layers in this experiment are in good agreement with values measured between single crystals containing about 0.2 wt% water (Helpa et al. 2014; **Table 2; Fig. 1**). Therefore, the presence of water appears to have no effect on the diffusion-controlled growth kinetics of Dol and Mg-Cal, at least between 0.2 wt% and ≈0.5 wt% H_2O. This agrees with deformation experiments on Carrara marbles, which are only weakly affected by the presence of water in the dislocation creep regime (de Bresser et al. 2005). To our knowledge, the influence of water on Ca or Mg self- or grain boundary diffusion in Cal or Dol has not been investigated. Self-diffusion experiments of C and O in Cal at T = 650–850 °C under dry conditions showed diffusion coefficients of similar orders of magnitude (Anderson 1969). In the presence of water, carbon self-diffusion coefficients remained similar, while self-diffusion of oxygen was accelerated by about 2 orders of magnitude at 750 °C (Kronenberg et al. 1984). This indicates that O-diffusion is not rate-limiting in our experiments, since we observed no influence of water in our rim growth experiments.

In contrast, in the silicate systems MgO-SiO_2 and Mg_2SiO_4-SiO_2, enhanced reaction rim growth kinetics were observed in the presence of water. Compared to nominally dry conditions, grain boundary diffusion was faster by a factor of 5 to 30 (Yund 1997; Gardés et al. 2012; Milke et al. 2013). Here, only trace amounts of water (tens of ppm) are necessary to enhance the reaction rates (Gardés et al. 2012; Milke et al. 2013). It is clear that due to the breaking of Si-O bonds in the presence of water and the formation of silanol groups, the silicate system is much more sensitive to the presence of water than Ca-Mg interdiffusion in the carbonate system.

Grain size and CPO development

Independent of deformation conditions, we observed grain growth in all polycrystalline starting materials as well as nucleation and growth of reaction products (**Tables 2, 3**).

Assuming an exponent of $n = 3$ for the grain growth law (e.g., Olgaard and Evans 1986, **eq. 3**), the growth rate constant K of Soln is in the range 5-8 × 10^{-3} µm³/s. The grain growth rate for poly-Mgs is 1-2 × 10^{-2} µm³/s, indicating faster grain growth for poly-Mgs compared to Soln (**eq. 3**). For comparison, Davis et al. (2011) determined grain growth rates of fine-grained, high purity Ca-Mg carbonates at $T = 800$ °C, $P = 300$ MPa, with rate constants of $K \approx 5 \times 10^{-1}$ µm³/s for calcite, $K \approx 3 \times 10^{-4}$ µm³/s for magnesite and $K \approx 5 \times 10^{-5}$ µm³/s for Dol. The Soln rate constant is ≈2 orders of magnitude lower and the poly-Mgs rate constant is ≈2 orders of magnitude higher compared to our experiments. This may be due to differences in the temperature of the experiments, porosity and impurity content of the starting materials. Assessment of the results reported by Davis et al. (2011) suggests only a minor effect of temperature differences. However, the porosity of our samples was 4% compared to 0.04% for samples used by Davis et al. (2011). Porosity of our magnesite samples was 6% compared to 28% in samples of Davis et al. (2011), revealing a strongly reduced growth rate at high porosity (Olgaard and Evans 1986; Herwegh el al. 2011).

The CPO development of Dol between polycrystalline reactants during deformation is independent of the starting materials' CPO. In torsion experiments, **c**-axes of Dol form girdles lying inclined at 45° with respect to the direction of shear. This corresponds to the direction of minimum or maximum principle stresses. Helpa et al. (2015) reported a similar rotation of Dol and Mg-Cal CPO's towards the compression or rotation axes (parallel to GD) during triaxial compression and twisting of Cal and Mgs. The CPO development results from deformation of the reaction product. We suggest that deformation was accommodated by a combination of diffusion creep, grain boundary sliding and dislocation activity (Delle Piane et al. 2007, 2008; Helpa et al. 2014). However, no evidence was found for any effect of the textural change on the reaction kinetics of Dol and Mg-Cal formation.

Implications

Our study shows that the kinetics of Dol- and Mg-Cal-forming reactions in carbonate systems are strongly affected by the grain size of the reactant phases. The formation of dolomite is enhanced by small magnesite grain sizes and Mg-Cal formation is enhanced by fine-grained calcite reactants. Similarly, growth rates of spinel forming between periclase and polycrystalline corundum were faster compared to spinel formed between single crystals of corundum and periclase (Keller et al. 2010). Likewise, formation of enstatite between quartz and olivine is enhanced if reactants are polycrystalline materials rather than single crystals (Götze et al. 2010). Compared to the strong effect of the reactant grain size on growth rates of reaction products, the effect of increased differential stress is insignificant.

In natural shear zones containing fine-grained ultramylonites, it is frequently found that the rates of metamorphic reactions are enhanced compared to the undeformed and typically coarser grained wall rocks (e.g., Kenkmann and Dresen 2002). The results suggest that high reaction rates are deformation-induced via grain size reduction of the reactant phases by dynamic recrystallization and/or cataclasis rather than via a stress-induced enhancement of component diffusion within the product phase. If fluids are present within shear zones, enhanced diffusion rates and solution-precipitation processes may further accelerate this effect.

Acknowledgements

We are grateful to P. Jeřábek and J. Till for discussions, S. Gehrmann for sample preparation, M. Naumann for technical support with the Paterson apparatus, H.-P. Nabein for XRD analyses and D. Rhede for help with the microprobe. Andreas Kronenberg, John Ferry and one anonymous reviewer are thanked for their valuable comments and suggestions. This work was funded by the Deutsche Forschungsgemeinschaft within the framework of FOR 741, project RY 103/1-1, which is gratefully acknowledged.

References

Althoff, P.L. (1977) Structural refinements of dolomite and a magnesian calcite and implications for dolomite formation in the marine environment. American Mineralogist, 62, 772-783.

Anderson, T.F. (1969) Self-Diffusion of carbon and oxygen in calcite by isotope exchange with carbon dioxide. Journal of Geophysical Research 74, 3918-3932.

Covey-Crump, S.J. (1997) The normal grain growth behaviour of nominally pure calcitic aggregates. Contributions to Mineralogy and Petrology, 129, 239-254.

Davis, N.E., Newman, J., Wheelock, P.B., and Kronenberg, A.K. (2011) Grain growth kinetics of dolomite, magnesite and calcite: A comparative study. Physics and Chemistry of Minerals, 38, 123-138.

de Bresser, J.H.P, Urai, J.L., and Olgaard, D.L. (2005) Effect of water on the strength and microstructure of Carrara marble axially compressed at high temperature. Journal of Structural Geology, 27, 265-281.

de Ronde, A.A., Heilbronner, R., Stünitz, H., and Tullis, J. (2004) Spatial correlation of deformation and mineral reaction in experimentally deformed plagioclase–olivine aggregates. Tectonophysics, 389, 93-109.

de Ronde, A.A., Stünitz, H., Tullis, J., and Heilbronner, R. (2005) Reaction-induced weakening of plagioclase–olivine composites. Tectonophysics, 409, 85-106.

de Ronde, A.A., and Stünitz, H. (2007) Deformation-enhanced reaction in experimentally deformed plagioclase-olivine aggregates. Contributions to Mineralogy and Petrology, 153, 699-717.

Delle Piane, C., Burlini, L., and Grobety, B. (2007) Reaction-induced strain localization: Torsion experiments on dolomite. Earth and Planetary Science Letters, 256, 36-46.

Delle Piane, C., Burlini, L., Kunze, K., Brack, P., and Burg, J.P. (2008) Rheology of dolomite: Large strain torsion experiments and natural examples. Journal of Structural Geology, 30, 767-776.

Deer W.A., Howie R.A., and Zussman J. (1992) An introduction to the rock- forming minerals, 2nd edn. Addison Wesley Longman Limited, Essex, 696 p.

Dohmen, R., and Milke, R. (2010) Diffusion in Polycrystalline Materials: Grain Boundaries, Mathematical Models, and Experimental Data. Reviews in Mineralogy and Geochemistry. 72, 921-970.

Farver, J.R., and Yund, R.A. (1996) Volume and grain boundary diffusion of calcium in natural and hot-pressed calcite aggregates. Contributions to Mineralogy and Petrology, 123, 77-91.

Fitz Gerald, J.D., and Stünitz, H. (1993) Deformation of granitoids at low metamorphic grade. I: Reactions and grain size reduction. Tectonophysics, 221, 269-297.

Gardés, E., and Heinrich, W. (2011) Growth of multilayered polycrystalline reaction rims in the MgO-SiO_2 system, part II: modeling, 162, 37-49.

Gardés, E., Wunder, B., and Marquardt, K. (2012) The effect of water on intergranular mass transport: new insights from diffusion-controlled reaction rims in the MgO–SiO_2 system. 164, 1-16.

Götze, L.C., Abart, R., Rybacki, E., Keller, L.M., Petrishcheva, E., and Dresen, G. (2010) Reaction rim growth in the system MgO-Al_2O_3-SiO_2 under uniaxial stress. Mineralogy and Petrology, 99, 263-277.

Haas, H. (1972) Diaspore-corundum equilibrium determined by epitaxis of diaspore on corundum. American Mineralogist, 57, 1375-1385.

Helpa, V., Rybacki, E., Abart, R., Morales, L.F.G, Rhede, D., Jeřábek, P., and Dresen, G. (2014) Reaction kinetics of dolomite rim growth. Contributions to Mineralogy and Petrology, 167, 1001.

Helpa, V., Rybacki, E., Morales, L.F.G, and Dresen, G. (2015) Influence of stress and strain on dolomite rim growth: a comparative study. Contributions to Mineralogy and Petrology, 170, 16.

Herwegh, M., Linckens, J., Ebert, A., Berger, A., and Brodhag, S.H. (2011) The role of second phases for controlling microstructural evolution in polymineralic rocks: A review. Journal of Structural Geology, 33, 1728, 1750.

Hirth, G., Teyssier, C., and Dunlap, W.J. (2001) An evaluation of quartzite flow laws based on comparisons between experimentally and naturally deformed rocks. International Journal of Earth Science, 90, 77–87.

Holyoke, C.W. III, and Tullis, J. (2006) The interaction between reaction and deformation: An experimental study using a biotite + plagioclase + quartz gneiss. Journal of Metamorphic Geology, 24, 743-762.

Holyoke, C.W. III, Kronenberg, A.K., Newman, J., and Ulrich, C. (2014) Rheology of magnesite. Journal of Geophysical Research Solid Earth, 119, 6534-6557.

Joachim, B., Gardés, E., Abart, R., and Heinrich, W. (2010) Experimental growth of åkermanite reaction rims between wollastonite and monticellite: evidence for volume diffusion control. Contributions to Mineralogy and Petrology, 161, 389-399.

Kenkmann, T., and Dresen, G. (2002) Dislocation microstructure and phase distribution in a lower crustal shear zone – an example from the Ivrea-Zone, Italy. International Journal of Earth Science, 91, 445-458.

Keller, L.M., Götze, L.C., Rybacki, E., Dresen, G., and Abart, R. (2010) Enhancement of solid-state reaction rates by non-hydrostatic stress effects on polycrystalline diffusion kinetics. American Mineralogist, 95, 1399-1407.

Kronenberg, A.K., Yund, R.A., and Giletti, B.J. (1984) Carbon and oxygen diffusion in calcite: Effets of Mn content and P_{H_2O}.

Llana-Fúnez, S., and Rutter, E.H. (2014) Effect of strain geometry on the petrophysical properties of plastically deformed aggregates: experiments on Solnhofen limestone. In S. Llana-Funez, A. Marcos, F. Bastida, Eds., Deformation structures and processes within the continental crust, 394, 167-187. Geological Society, London, Special Publication.

Milke, R., Neusser, G., Kolzer, K., and Wunder, B. (2013) Very little water is necessary to make a dry solid silicate system wet. Geology, 41, 247-250.

Newman, J., Lamb, W.M., Drury, M.R., and Vissers, R.L.M. (1999) Deformation processes in a peridotite shear zone: reaction-softening by an H_2O-deficient, continuous net transfer reaction. Tectonophysics, 303, 193-222.

Olgaard, D.L., and Evans, B. (1986) Effect of second-phase particles on grain growth in calcite. Journal of American Ceramic Society, 69, C-272-C-277.

Olgaard, D.L., and Evans, B (1988) Grain growth in synthetic marbles with added mica and water. Contributions of Mineralogy and Petrology, 100, 246-260.

Post, A.D., Tullis, J., and Yund, R.A. (1996) Effects of chemical environment on dislocation creep of quartzite. Journal of Geophysical Research,101, 22143-22155.

Rubie, D.C. (1983) Reaction-enhanced ductility: The role of solid-solid univatiant reactions in deformation of the crust and mantle. Tectonophysics, 96, 331-352.

Rutter, E.H., and Brodie, K.H. (1988) Experimental "syntectonic" dehydration of serpentinite under conditions of controlled pore water pressure. Journal of Geophysical Research, 93, 4907-4932.

Rutter, E.H., and Brodie, K.H. (2004) Experimental intracystalline plastic flow in hot-pressed synthetic quartzite prepared from Brazilian quartz crystals. Journal of Structural Geology, 26, 259-270.

Rybacki, E., Evans, B., Janssen, C., Wirth, R., and Dresen, G. (2013) Influence of stress, temperature, and strain on calcite twins constrained by deformation experiments. Tectonophysics, 601, 20-36.

Schmid, S.M., Boland, J.N., and Paterson, M.S. (1977) Superplastic flow in finegrained limestone. Tectonophysics, 43, 257-291.

Tsurumi, J., Hosonuma, H., and Kanagawa, K. (2003) Strain localization due to a positive feedback of deformation and myrmekite-forming reaction in granite and aplite mylonites along the Hatagawa Shear Zone of NE Japan. Journal of Structural Geology, 25, 557-574.

Underwood, E.E. (1970) Quantitative Stereology. Addison-Wesley Publishing Company, Boston, Massachusetts, p. 274.

Yund, R.A. (1997) Rates of grain boundary diffusion through enstatite and forsterite reaction rims. Contributions to Mineralogy and Petrology, 126, 224-236.

Figure 1. Schematic diagram of reaction product widths in samples annealed for 29 h. Widths of the entire dolomite reaction rim Δx_{Dol} (*light grey*) and magnesio-calcite layer $\Delta x_{Mg\text{-}Cal}$ (*intermediate grey*) are given between different starting materials (top and bottom). The *dashed line* represents the initial contact of starting materials. *Dark grey* boxes indicate dolomite rims, where no initial contact interface could be determined. In the first column, measured values are listed and ±1 standard deviation uncertainties are given by error bars at phase boundaries. Following columns are normalized with respect to the first column. Measurements of the corresponding experiments are from **Table 2**. Asterisk (*) indicates annealing experiment performed by Helpa et al. (2014).

Figure 2. Schematic diagram of reaction product width in samples deformed for 18 h. For detailed information, see **Figure 1**.

Asterisks(*) indicate results of 1) torsion experiment by Helpa et al. (2015) and 2) annealing experiment performed by Helpa et al. (2014). In torsion experiment of Helpa et al. (2015), a decrease in Dol rim Mg-Cal layer thickness was observed with increasing strain.

Figure 3. Optical micrographs of Dol and Mg-Cal between different starting materials formed during static annealing at 750 °C for 29 h in stack-01. Starting materials are **a-b** Soln/poly-Mgs, **c-d** poly-Mgs/Cal, **e-f** Cal/Mgs and **g** Mgs/Soln. Phase boundaries are shown by *solid lines* and the initial contact of the starting material is indicated by the *dashed line*. *Dotted line* in **g** indicates the petrographic boundary between Mg-Cal and Soln. In the right column corresponding close-ups of the Dol microstructures are shown. Note different scales.

Figure 4. Backscattered electron image of reaction products between polycrystalline starting materials in twisted sample pCa_pMg-01. Grain boundaries of Soln and Mg-Cal are decorated by dolomite as indicated by the *white arrows*.

Figure 5. Backscattered electron (BSE) images and chemical profiles of reaction products between **a** Cal and poly-Mgs and **b** poly-Mgs and Soln from experiment stack-01 (*t* = 29, annealed). Values of X_{Ca} and X_{Mg} across the reaction rim are given in *red* and *black*, respectivley. *Solid vertical lines* represent phase boundaries and *dashed lines* indicate the location of the initial interface between reactants. *White arrows* in **b** indicate dolomite formation associated with pores.

Figure 6. BSE images and chemical profiles of torsion experiment Ca_pMg-02, including Cal and poly-Mgs. Values of X_{Ca} and X_{Mg} are illustrated as in **Fig. 5**. Line scans were done at different locations within the sample representing a certain shear stress/strain condition. Shown are **a** the central part of the sample ($\tau \approx 0.7$ MPa; $\gamma \approx 0.1$), **b** a location further away from the center ($\tau \approx 1$ MPa; $\gamma \approx 1.9$) and **c** at the edge of the sample ($\tau \approx 1$ MPa, $\gamma \approx 3.4$).

Figure 1

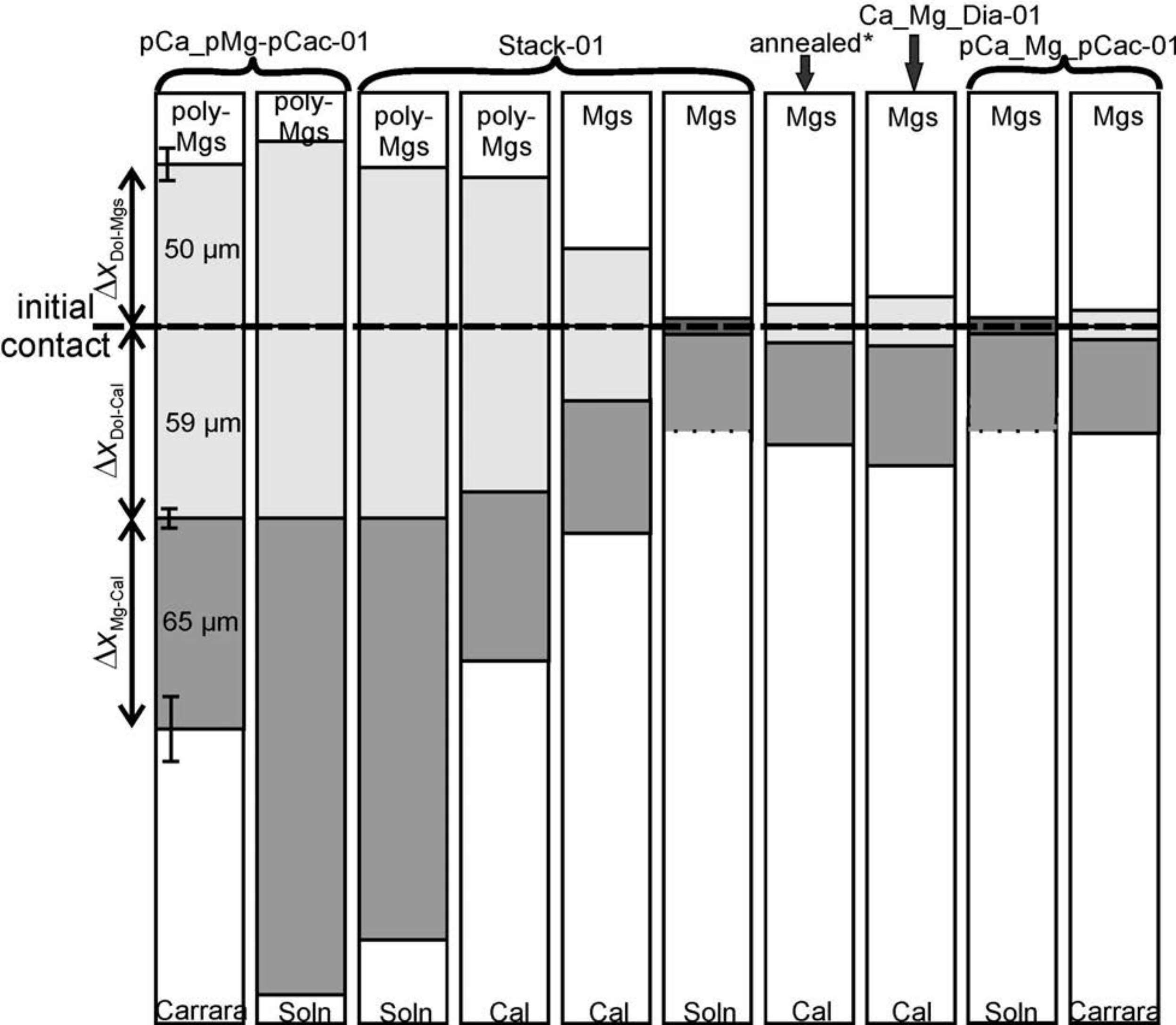
pCa_pMg-pCac-01
Stack-01
Ca_Mg_Dia-01
annealed*
pCa_Mg_pCac-01
poly-Mgs
poly-Mgs
poly-Mgs
poly-Mgs
Mgs
Mgs
Mgs
Mgs
Mgs
Mgs
$\Delta x_{Dol\text{-}Mgs}$
50 µm
initial contact
$\Delta x_{Dol\text{-}Cal}$
59 µm
$\Delta x_{Mg\text{-}Cal}$
65 µm
Carrara
Soln
Soln
Cal
Cal
Soln
Cal
Cal
Soln
Carrara

Figure 2

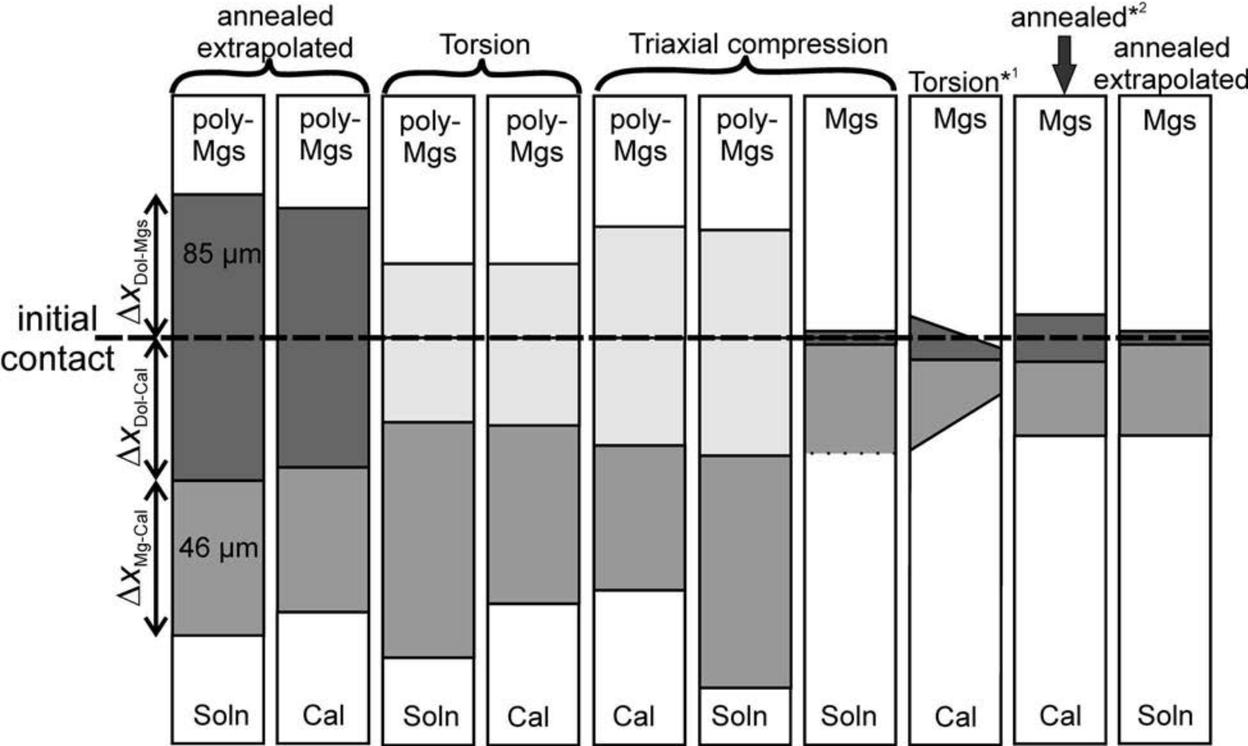
annealed
extrapolated
Torsion
Triaxial compression
Torsion*1
annealed*2
annealed
extrapolated
poly-Mgs
poly-Mgs
poly-Mgs
poly-Mgs
poly-Mgs
poly-Mgs
Mgs
Mgs
Mgs
Mgs
initial contact
ΔX Dol-Mgs
85 µm
ΔX Dol-Cal
ΔX Mg-Cal
46 µm
Soln
Cal
Soln
Cal
Cal
Soln
Soln
Cal
Cal
Soln

Figure 3

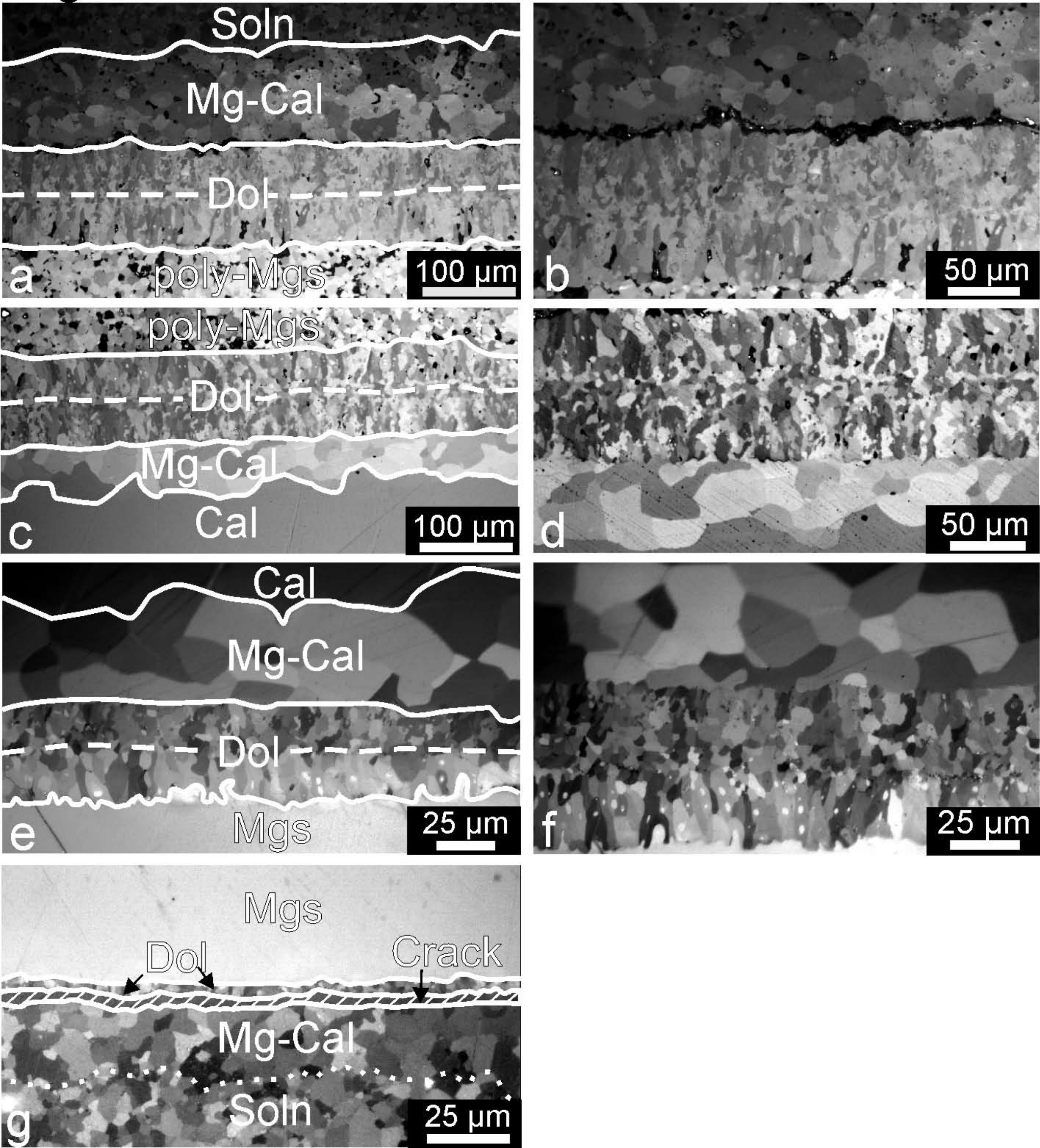
Soln
Mg-Cal
Dol
poly-Mgs
100 µm
a
50 µm
b
poly-Mgs
Dol
Mg-Cal
Cal
100 µm
c
50 µm
d
Cal
Mg-Cal
Dol
Mgs
25 µm
e
25 µm
f
Mgs
Dol
Crack
Mg-Cal
Soln
25 µm
g

Figure 4

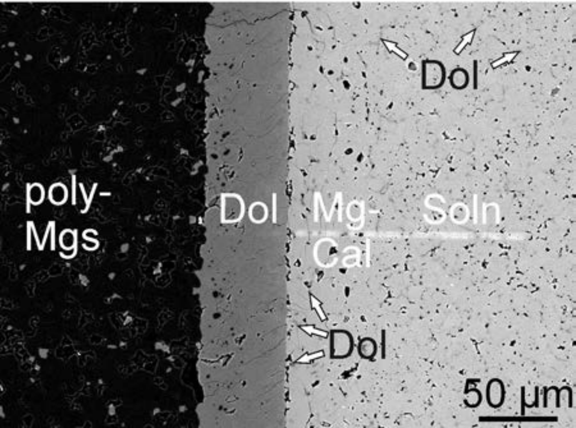

Figure 5

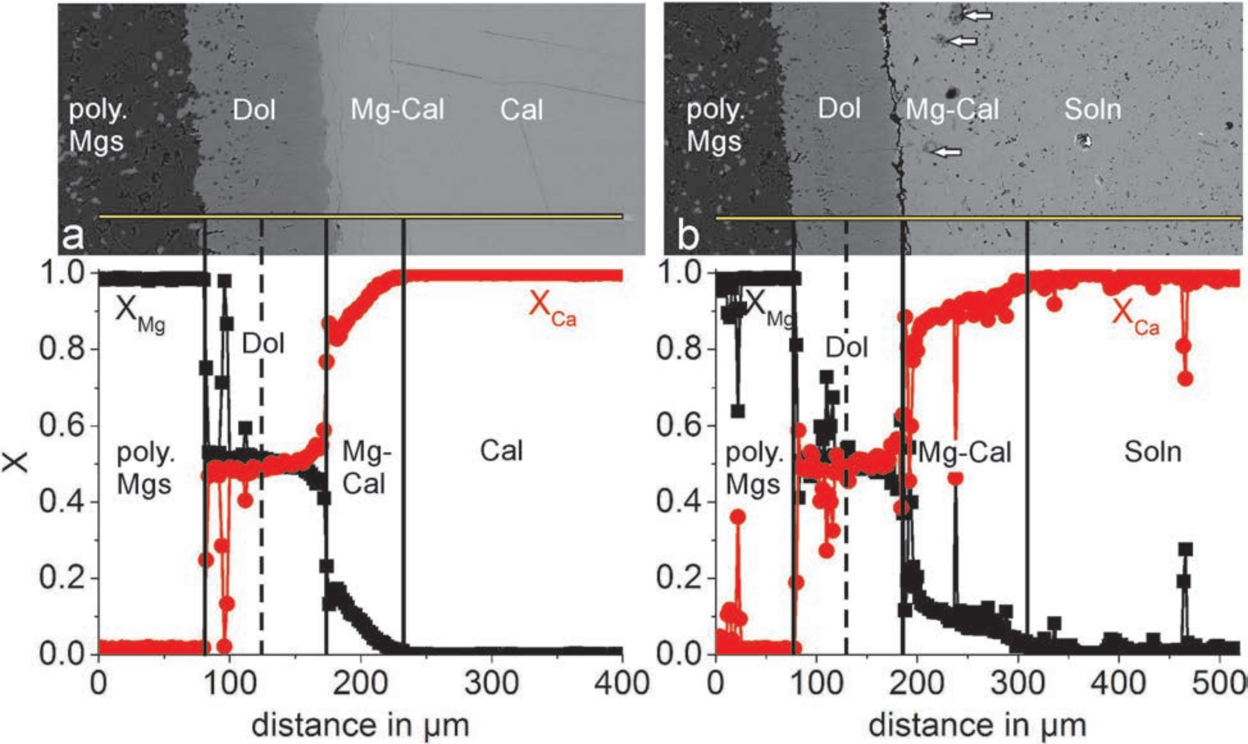

poly. Mgs
Dol
Mg-Cal
Cal
a
poly. Mgs
Dol
Mg-Cal
Soln
b
1.0
0.8
0.6
0.4
0.2
0.0
X
X_{Mg}
X_{Ca}
Dol
poly. Mgs
Mg-Cal
Cal
Mg-Cal
Soln
0
100
200
300
400
500
distance in µm
distance in µm

Figure 6

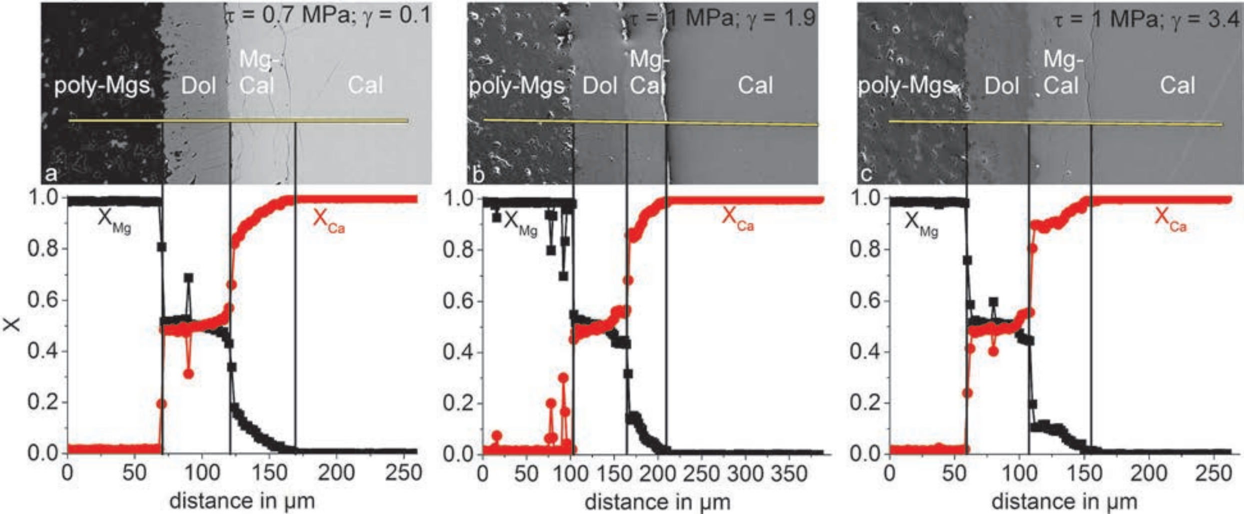
τ = 0.7 MPa; γ = 0.1
poly-Mgs
Dol
Mg-Cal
Cal
a
τ = 1 MPa; γ = 1.9
poly-Mgs
Dol
Mg-Cal
Cal
b
τ = 1 MPa; γ = 3.4
poly-Mgs
Dol
Mg-Cal
Cal
c
X
1.0
0.8
0.6
0.4
0.2
0.0
X_{Mg}
X_{Ca}
0
50
100
150
200
250
300
350
distance in µm

Table 1. Starting material assemblies (from top to bottom) and experimental conditions. All experiments were performed at 750 °C temperature and 400 MPa confining pressure. t is time, ε is bulk axial strain and $\dot{\varepsilon}$ is strain rate measured in triaxial compression at constant axial stress σ_{max}. τ_{max} is the maximum shear stress and γ is the maximum shear strain obtained in torsion experiments at constant shear strain rate $\dot{\gamma}$. Uncertainties of measurements are given in parentheses.

Experiment	**Starting assembly**	***t*** **(h)**	**Strain**	**Strainrate (s^{-1})**	**Stress (MPa)**
annealing			ε	$\dot{\varepsilon}$	σ_{max}
Stack-01	Soln/Mgs/Cal /poly-Mgs/Soln	29	-	-	-
pCa_Mg_pCac-01	Soln/Mgs/Carrara	29	-	-	-
Ca_Mg_Dia-01	Mgs/Cal	29	-	-	-
pCa_pMg_pCac-01	Soln/poly-Mgs/Carrara	29	-	-	-
Triaxial					
Ca_pMg_pCa_Mg-01	Cal/poly-Mgs/Soln/Mgs	18	0.17	1×10^{-4}	20 (for 0.5 h)
Torsion			γ	$\dot{\gamma}$	τ_{max}
pCa_pMg-01	Soln/poly-Mgs	18	2	3.1×10^{-5}	3.8(5)
Ca_pMg-02	Cal /poly-Mgs	18	4	6.2×10^{-5}	1.7(4)

Note: Soln = Solnhofen limestone, Mgs = magnesite single crystal, Cal = calcite single crystal, poly-Mgs = polycrystalline magnesite, Carrara = Carrara marble.

Table 2. Measured average layer thicknesses of the entire polycrystalline dolomite layer (Δx_{Dol}), dolomite formed in contact with magnesite ($\Delta x_{Dol\text{-}Mgs}$), dolomite formed in contact with magnesio-calcite ($\Delta x_{Dol\text{-}Cal}$) and magnesio-calcite ($\Delta x_{Mg\text{-}Cal}$). The mean grain diameters of the dolomite and magnesio-calcite grains are represented by $a_{Dol\text{-}Mgs}$, $a_{Dol\text{-}Cal}$, and $a_{Mg\text{-}Cal}$. One standard deviation of measurements in parentheses. The fraction ν_{Mg} is the molar amount of Mg relative to Ca+Mg transferred across the initial contact interface (see **eq. 2**).

Experiment	**interfaces**	***t*** **(h)**	**Δx_{Dol} (μm)**	**$\Delta x_{Dol\text{-}Mgs}$ (μm)**	**$\Delta x_{Dol\text{-}Cal}$ (μm)**	**$\Delta x_{Mg\text{-}Cal}$ (μm)**	**$a_{Dol\text{-}Mgs}$ (μm)**	**$a_{Dol\text{-}Cal}$ (μm)**	**$a_{Mg\text{-}Cal}$ (μm)**	**ν_{Mg}**
annealing										
Stack-01	Soln/Mgs	29	5(1)	NA	NA	30_a	NA	NA	NA	NA
	Mgs/Cal		47(11)	24(6)	23(6)	41(9)	5.0(11)	4.5(10)	24.3(134)	0.54(9)
	Cal/poly-Mgs		98(7)	46(6)	51(4)	52(7)	6.9(13)	6.7(16)	28.4(117)	0.55(4)
	poly-Mgs/Soln		108(8)	49(6)	59(6)	130(13)	6.3(11)	5.7(10)	20.9(94)	0.60(4)
pCa_Mg_pCac-01	Soln/Mgs	29	5(1)	NA	NA	30_a	NA	NA	NA	NA
	Mgs/Carrara		9(2)	5(1)	4(1)	29(8)	2.1(5)	2.3(07)	17.1(108)	0.58(10)
Ca_Mg_Dia-01	Mgs/Cal	29	14(4)	9(2)	6(2)	37(10)	4.5(15)	4.2(16)	23.5(143)	0.51(10)
pCa_pMg_pCac-01	Soln/poly-Mgs	29	117(7)	57(5)	59(5)	147(14)	6.6(16)	5.7(16)	21.3(84)	0.57(NA)
	Poly-Mgs/Carrara		108(5)	50(5)	59(3)	65(10)	6.7(18)	5.4(20)	24.0(161)	0.56(NA)
Triaxial										
Ca_pMg_pCa_Mg-01	Cal/poly-Mgs	18	65(4)	33(3)	32(3)	43(5)	5.4(13)	5.0(13)	23.6(115)	0.53(4)
	poly-Mgs/Soln		67(4)	32(4)	35(4)	69(9)	6.0(17)	4.9(10)	21.3(72)	0.57(4)
	Soln/Mgs		4(1)	NA	NA	32_a	NA	NA	NA	NA
Torsion										
pCa_pMg-01	Soln/poly-Mgs	18	47(6)	22(3)	25(4)	70(19)	6.5(22)	6.4(22)	18.4(92)	0.60(6)
Ca_pMg-02	Cal/poly-Mgs	18	48(6)	22(4)	26(5)	53(9)	5.9(19)	6.3(19)	24.5(149)	0.60(8)

Note: The subscript *a* denotes thicknesses estimated by petrographically observations together with microprobe analyses. NA denotes "Not Available".

Table 3. Porosity and grain sizes for polycrystalline magnesite and Solnhofen limestone at different experimental conditions.

	Porosity (%)	**Grain size (µm)**
Polycrystalline magnesite		
Starting material	6	4(0)
29 h annealing	6.8	11(3)
18 h triaxial compression	6.8	11(2)
18 h torsion	10.8	10(3)
Solnhofen limestone		
Starting material	4	6(1)
29 h annealing	3.7	9(1)
18 h triaxial compression	3.7	9(1)
18 h torsion	3.1	9(1)